RESEARCH ARTICLE | APRIL 27 2023

Study of charge transport mechanism in Ba doped Sr₂CrMoO₆ double perovskite mixed ionic electronic conductor ⊘

Vivek Kumar ; Sudha Saini ; Tanmoy Maiti ✉

Check for updates

🌐
View
Online

Export
Citation

CrossMark

Study of charge transport mechanism in Ba doped Sr$_2$CrMoO$_6$ double perovskite mixed ionic electronic conductor

Vivek Kumar, [iD] Sudha Saini, [iD] and Tanmoy Maiti[a] [iD]

AFFILIATIONS

Plasmonics and Perovskites Laboratory, Department of Materials Science and Engineering, IIT Kanpur, Kanpur, Uttar Pradesh 208016, India

[a]**Author to whom correspondence should be addressed:** tmaiti@iitk.ac.in. **Telephone:** +91-512-259-6599.

ABSTRACT

In this work, the conduction mechanism in Ba$_x$Sr$_{2-x}$CrMoO$_6$ ($0 \leq x \leq 0.3$) double perovskite has been investigated using different techniques, such as universal dynamic response (UDR) and modulus spectroscopy. AC impedance spectroscopy has been studied in the frequency range of 0.3 Hz–5 MHz in a wide range of temperatures. It has been found that the conduction mechanism is thermally activated and frequency-dependent. The impedance fitting response to the microstructure reveals that grain boundaries are more resistive and capacitive than grains. Analysis of the complex modulus indicates that both short- and long-range charge carrier transport is responsible for conduction with non-Debye-type response in these oxides. The permittivity analysis indicates the existence of both universalities, near constant loss and UDR. Furthermore, from the Almond West power law, hopping frequency (ω_c) and activation energy E_a^c have been calculated. The relaxation time and DC conductivity are found to obey Barton Nakajima and Namikawa's relation. In addition, the Kramers–Kronig relation and conductivity scaling are discussed to validate the impedance data and provide insight into the conduction processes in this mixed ionic electronic conductor.

I. INTRODUCTION

Mixed ionic electronic conductors (MIECs) are state-of-the-art materials with the ability to conduct both matter (atoms/ions) and electronic charges (electrons/holes). MIECs have been used for various applications such as in batteries, sensors, catalysis, solid oxide fuel cells (SOFCs), etc.[1–4] SOFCs are electrochemical conversion devices that convert chemical energy directly to electrical energy with minimum environmental impact. They consist of mainly three components: a dense ion-conducting electrolyte and a set of porous electronic–ionic conducting anode and cathode. The ability of SOFCs to internal reforming of hydrocarbon-based fuels such as syngas, biomass, and municipal biowaste along with hydrogen makes it more adaptable as hydrogen generally comes from natural gas steam reforming and coal gasification.[5,6] MIEC electrodes, especially the anode, play a critical role in the internal fuel reforming process at the anode side by providing electronic and ionic conductivities while enhancing the catalytic surface available for anode reactions.[7]

These electrodes are often composed of double perovskite oxides.[8] These transition metal double perovskite oxides have the chemical formula of A$_2$BB$'$O$_6$, where A-atom can be alkali-earth metals (A = Sr, Cr, Ba, La, etc.) and B and B$'$ are transition metals.[9] The bigger A-cations are coordinated by 12 oxygen ions, and the B/B$'$-atom contains oxygen octahedra (BO$_3$ or B$'$O$_3$ octahedra) which can be distorted.[10] There has been tremendous development in the class of double perovskite oxide for various applications, including electronics and magnetism.[11–14] Moreover, A$_2$BB$'$O$_6$-based double perovskites are among the most promising SOFC electrode candidates owing to their high electronic and ionic conductivity, contamination tolerance, catalytic activity, and stability at higher temperatures.[9] For example, La$_{0.75}$Sr$_{0.25}$Cr$_{0.5}$Mn$_{0.5}$O$_{3-\delta}$ (LSCM) is one of the best-known anode materials with excellent stability in various fuels and the ability for methane oxidation which is comparable to the state-of-the-art Ni/YSZ cermet. However, it has low electronic conductivity and poor tolerance for a H$_2$S environment.[15–17] Similarly, Sr$_2$NiMoO$_{6-\delta}$ double perovskite has shown to be a promising SOFC anode material with a

power density of $819\,m\,Wcm^{-2}$ in a H_2 environment. With $La_{0.9}Sr_{0.1}Ga_{0.8}Mg_{0.2}O_3$ (LSGM) as the electrolyte and $Ba_{0.5}Sr_{0.5}Co_{0.8}Fe_{0.2}O_3$ (BSCF) as the cathode and without any buffer layer, the system did not undergo any unfavorable chemical reactions.[18] Furthermore, rare-earth doping (La) has been shown to enhance the conductivity and stability of the material in reducing the atmosphere.[19] But the conductivity and tolerance for sulfur and other contaminants are still inappropriate for SOFC electrode employment. Among the double perovskites, Mo-based materials have proven to be highly catalytically active along with enhanced conductivity due to the presence of Mo^{5+}/Mo^{6+} pairs.[15] Doping of Mo in $Pr_{0.5}Ba_{0.5}MnO_{3-\delta}$ has been shown to improve the oxygen vacancy concentration with improved catalytic activity for H_2 and CH_4.[20]

In the search for rare-earth free and cost-effective SOFC electrode material, herein we report the conductivity mechanism of chromium-based Sr_2CrMoO_6 (SCM) double perovskite. As a versatile material, SCM exhibits a wide range of properties such as giant linear magnetoresistance, an electrocatalyst for rechargeable lithium–air batteries, and SOFC electrodes.[12,15,21,22] Bonilla et al. were the first to perform density functional theory (DFT) calculations to analyze its electronic structure and they showed the half-metallic behavior of SCM.[23] In the current study, Ba-doped SCM, $Ba_xSr_{2-x}CrMoO_6$ with different compositions ($0 \leq x \leq 0.3$) were synthesized using the solid-state reaction method. Its microstructural and electrical properties have been investigated using x-ray diffraction (XRD) analysis, field emission scanning electron microscopy (FESEM), and electrochemical impedance spectroscopy (EIS). EIS is an excellent non-destructive technique to examine the frequency and temperature dependence of the conductivity of polycrystalline ceramics, polymers, glasses, etc.[24–26] In this study, it has been used to compare the polarization resistance and performance of electrode materials. Furthermore, in order to gain insight into the charge transport mechanism of these double perovskites, we adopted various techniques such as AC conductivity analysis using the Almond–West (AW) power law,[27] complex permittivity,[28] and complex modulus formalism.[29] Likewise, the Barton,[30] Nakajima,[31] and Namikawa[32] (BNN) relation and Kramers Kronig transformation[33] (KKT) were examined to verify the analysis of impedance data. The scaling behavior was further analyzed with the time-temperature superposition principle (TTSP) of ac conductivity.[34]

II. EXPERIMENTAL PROCEDURE

Polycrystalline samples were synthesized via a conventional solid-state reaction route. Starting reagents $SrCO_3$ (Sigma Aldrich $\geq 99.9\%$), MoO_3 (Sigma Aldrich $\geq 99.9\%$), Cr_2O_3 (Sigma Aldrich $\geq 99.9\%$), and $BaCO_3$ (Sigma Aldrich $\geq 99.9\%$) were taken. Stochiometric amounts of raw reagents were mixed using ball milling with zirconia balls. The obtained power was calcined at 1673 K for 10 h in the H_2 atmosphere. Again, calcined powders were ball milled in an alcohol medium using zirconia balls in a planetary micromill (Fritsch®, PULVERISETTE 7 premium Line, Germany). Cylindrical samples ($\sim 1.5 \times 15\,mm^2$) were prepared by uniaxial pressing and then compacted pellets were sintered at 1773K for 16h in the H_2 environment. Room temperature x-ray diffraction (XRD) was used for phase analysis using the PANalytical X'Pert diffractometer. Furthermore, background correction, thermal parameters, and

pseudo-Voigt profiles were performed on XRD data by Rietveld refinement using Fullprof software.[35] A microstructure study was performed using FESEM (Carl Zeiss NTS GmbH, EV050, Germany). Finally, AC impedance measurement was performed via an impedance analyzer (Solartron 1260 A, UK) with a 1286 Solartron electrochemical system. Complex impedance was studied from 0.3 Hz to 5 MHz with an applied AC amplitude of 500 mV in an 85% H_2 and a 15% N_2 environment. Electrochemical testing was performed in a vertical furnace where the samples were placed between spring-loaded alumina plates. A platinum plate was used as the electrode for current collection with every 50 °C temperature difference during the cooling cycle. Before testing, the samples were coated with a platinum paste and baked at 900 °C for 1h in the H_2 environment. The samples were named SCM, 1BSCM, and 3BSCM for the composition $Ba_xSr_{2-x}CrMoO_6$, where $x = 0$, 0.1, and 0.3, which correspond to $Sr_2 CrMoO_6$, $Ba_{0.1}Sr_{1.9} CrMoO_6$, and $Ba_{0.3}Sr_{1.7} CrMoO_6$, respectively.

The AC response of the samples was studied in a complex impedance plot. These responses can be further formulated in four fundamental parameters, which are complex admittance (Y*), complex impedance (Z*), complex modulus (M*), and complex permittivity (ε^*). They are expressed as[36,37]

$$Y^* = \left(\frac{A}{d}\right)\sigma^* = \frac{A}{d}(\sigma' + \sigma'') = \frac{1}{Z^*} = j\omega C_0 \varepsilon^*, \quad (1)$$

$$Z^* = Z' + jZ'', \quad (2)$$

$$M^* = (\varepsilon^*)^{-1} = j\omega C_0 Z^* = M' + jM'', \quad (3)$$

$$\varepsilon^* = \varepsilon' + j\varepsilon'', \quad (4)$$

where Z' and Z'' are the real and imaginary parts of complex impedance, respectively. Similarly, M', M'', ε', and ε'' are the real and imaginary parts of complex modulus and complex permittivity, respectively. ω is the angular frequency in rad/s, C_0 ($= \varepsilon_0 \frac{A}{d}$) is vacuum capacitance, $\varepsilon_0 = 8.854 \times 10^{-12}$ F/m, and $j = \sqrt{-1}$. A and d represent the area and thickness of the sample, respectively.

III. RESULT AND DISCUSSION

A. Structural and microstructure analysis

1. X-ray diffraction analysis

After sintering the samples, XRD was employed to confirm phase purity and crystal structure. Figure 1 shows the XRD pattern of samples wherein no impurity peak was found for 1BSCM and 3BSCM. However, a small impurity phase around 40.8° was observed for pure SCM, which may be due to the Sr_2CrO_4 phase. The absence of a secondary phase indicates the formation of a single-phase solid solution of Ba-doped Sr_2CrMoO_6 double perovskite, as shown schematically in Fig. 1(a). Moreover, Rietveld refinement was performed to ascertain crystallographic information, such as lattice parameters and space groups of different samples. All the XRD data were fitted with $Pm\bar{3}m$ space group with a very low χ^2 value showing excellent fitting, as shown in Table I. The pure SCM sample shows the least lattice parameter of 3.92 Å.
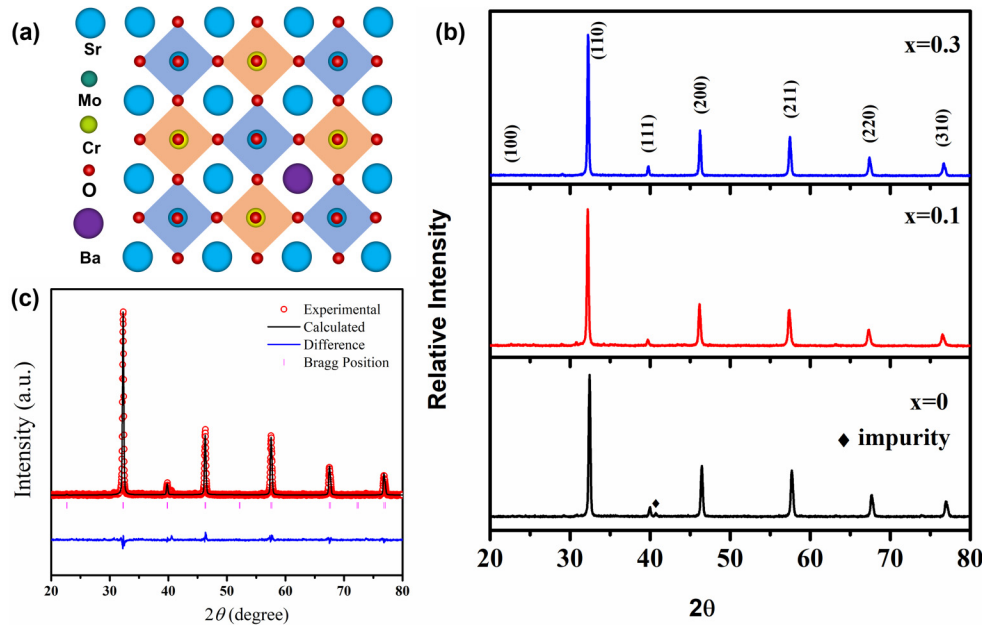
FIG. 1. (a) Schematic showing the crystallographic projection of $Ba_x Sr_{2-x} CrMoO_6$ double perovskite, (b) XRD of $Ba_x Sr_{2-x} CrMoO_6$ (x = 0.0, 0.1 and 0.3), and (c) Rietveld refinement fitted XRD pattern of $Ba_{0.1}Sr_{1.9} CrMoO_6$ sample.

The addition of a larger Ba atom (ionic radius = 1.61 Å) compared to Sr (ionic radius = 1.44 Å) resulted in an increased lattice parameter as compared to pure SCM.

2. Field emission scanning electron microscopy (FESEM)

Figure 2 shows the FESEM image of $Ba_xSr_{2-x}CrMoO_6$ samples of different compositions. The microstructure obtained had good porosity for x = 0.0, 0.1, and 0.3. The grains were predominantly spherical in shape, and the average grain size was calculated using ImageJ software.[38] The averaged grain size for SCM, 1BSCM, and 3BSCM were found to be 1.19, 1.05, and 1.03 μm, respectively. It can be seen that Ba-doping led to a decrease in the grain size of SCM.

B. Complex electrochemical impedance spectroscopy (EIS)

Impedance spectroscopy is a non-destructive electrochemical technique that is generally employed to understand the electrical properties of ceramics, polymers, batteries, corrosion behavior, etc.[39] EIS utilizes a low-amplitude AC signal over a frequency range and measures its electrical response in a wide frequency spectrum. Electrochemical systems are studies in analogs to an electrical circuit in which resistors, capacitors, inductors, etc., are designated to understand the underlying mechanisms.

Figure 3(d) represents the Nyquist plot at 773 K for all samples for which EIS Spectrum Analyser software was used for fitting the impedance data.[40] The Nyquist data were divided into three regions in which the high-frequency ($\geq 10^5$ Hz), medium-frequency ($< 10^5$ Hz), and low-frequency ($< 10^3$ Hz) responses were assigned as a contribution from grain, grain boundary, and electrode polarization.[36] The data were fitted with the (L)-(R_g, CPE_g)-(R_{gb}, CPE_{gb}) model, where L, R_g, and R_{gb} represent inductor, grain, and grain boundary resistance, respectively. CPE stands for constant phase elements and represents non-ideal capacitors which account for non-homogeneity in the system. Capacitance (C_g and C_{gb}) from CPE is calculated using $C = (R^{1-n} \times Q)^{1/n}$, where Q and n are parameters of the CPE elements.[40] The grain boundaries ($\sim 10^{-10}$ F) are found to be more capacitive than grains ($\sim 10^{-11}$ F) for every compositions

TABLE I. Lattice parameter and χ^2 value from Rietveld refinement and the average grain size of $Ba_xSr_{2-x}CrMoO_6$ (x = 0.0, 0.1, and 0.3) samples.

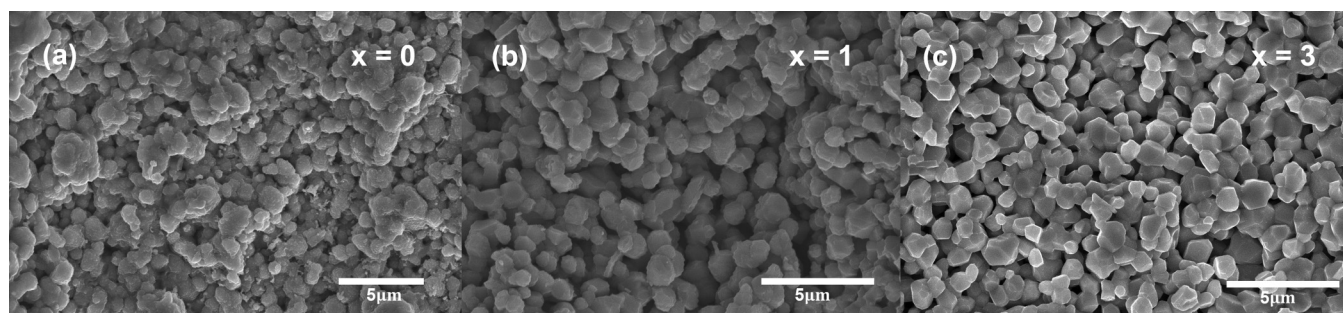| Compositions	Lattice parameter (Å)	R_p	R_{wp}	R_{exp}	R_f	χ^2	Avg. grain size (μm)
Sr_2CrMoO_6	3.9213	26.3	26.6	18.96	10.9	1.97	1.19
$Ba_{0.1}Sr_{1.9}CrMoO_6$	3.9337	21.2	21.8	16.02	9.06	1.84	1.05
$Ba_{0.3}Sr_{1.7}CrMoO_6$	3.9336	18.7	20.7	15.48	8.74	1.78	1.03

FIG. 2. Microstructure of the fracture surface of $Ba_xSr_{2-x}CrMoO_6$ (BSCM) double perovskite for (a) x = 0, (b) x = 0.1, and (c) x = 0.3 compositions, respectively.
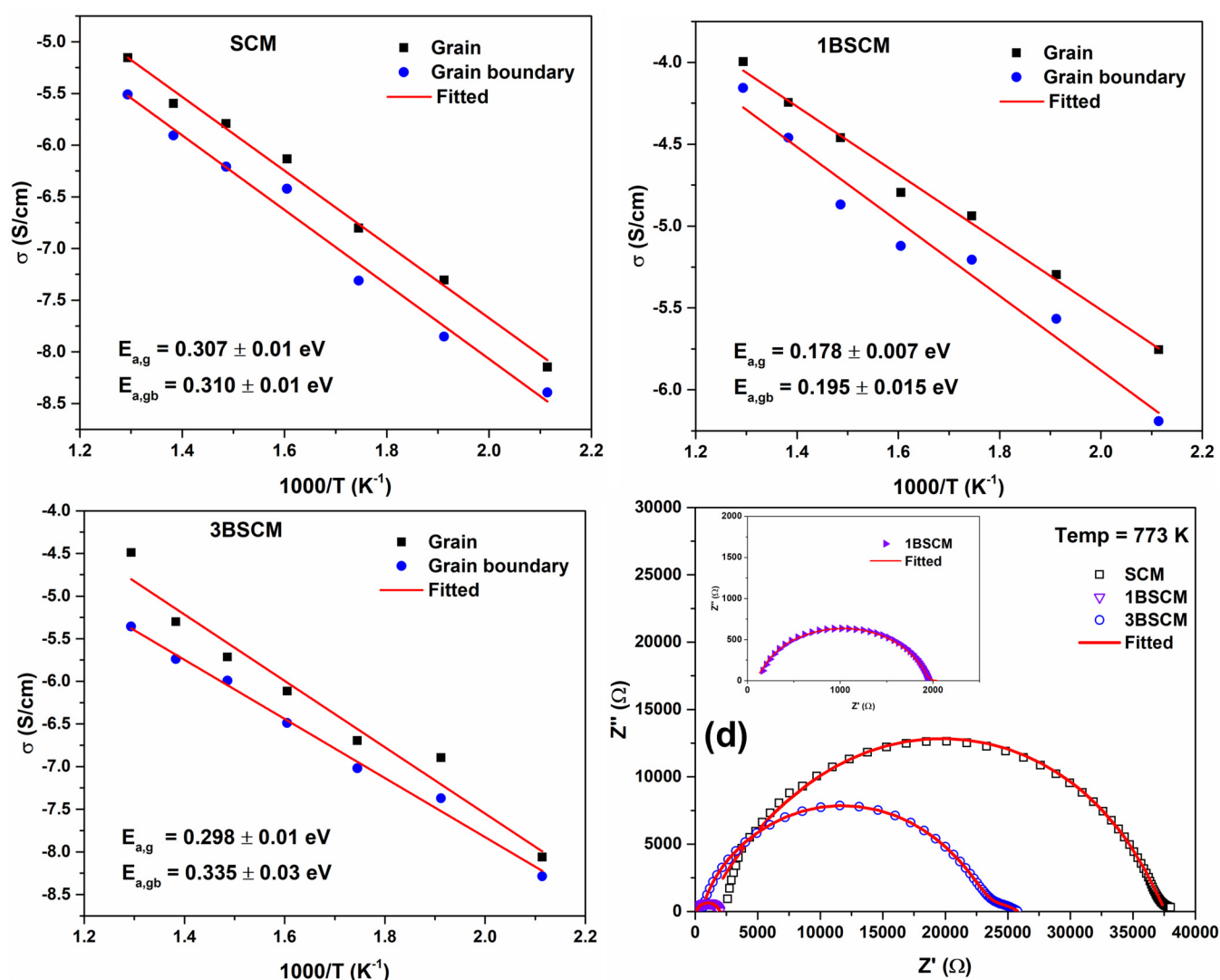

FIG. 3. Arrhenius plot of conductivity vs 1000/T for (a) SCM, (b) 1BSCM, and (c) 3BSCM; (d) electrochemical impedance data fitting at 773 K of BSCM samples.

TABLE II. Obtained grain and grain boundary conductivities for different samples at 773 K.

SCM ($\times 10^{-3}$ mS cm^{-1})		1BSCM ($\times 10^{-3}$ mS cm^{-1})		3BSCM ($\times 10^{-3}$ mS cm^{-1})	
σ_g	σ_{gb}	σ_g	σ_{gb}	σ_g	σ_{gb}
7.04 ± 0.14	3.09 ± 0.06	104.17 ± 2.08	71.94 ± 1.4	33.33 ± 0.66	4.4 ± 0.088

at all temperatures under investigation. It was found that with increasing temperature, the arc of the Nyquist plot decreases, showing an increase in conductivity. The relation between impedance, capacitance, and resistance can be given as

$$Z' = \frac{R_g}{1 + (\omega R_g C_g)^2} + \frac{R_{gb}}{1 + (\omega R_{gb} C_{gb})^2}, \tag{5}$$

$$Z'' = R_g\left(\frac{\omega R_g C_g}{1 + (\omega R_g C_g)^2}\right) + R_{gb}\left(\frac{\omega R_{gb} C_{gb}}{1 + (\omega R_{gb} C_{gb})^2}\right). \tag{6}$$

The conductivity of grain boundaries was found to be lower than grains for all the compositions. Moreover, the doping of Ba-cation enhanced the grain and grain boundary conductivity by 15 and 23 folds at 773 K, respectively. The 1BSCM sample showed maximum conductivity at all temperature ranges, but further doping resulted in a decrease in conductivity, as shown in Table II. The enhanced electrical conductivity for 1BSCM composition can be attributed to increased charge carrier's mobility. The maximum grain and grain boundary conductivity for 1BSCM at 773 K was found to be 0.10 and 0.071 mS cm^{-1}, respectively. However, further doping lowers electrical conductivity, which might be attributed to enhanced strain and polarization in the materials due to the size difference between Sr^{+2} and Ba^{+2} ions. This could lead to an increased barrier, which may inhibit the conduction path and lead to the accumulation of charge carriers in the grain and grain boundary region.[41] It has been discussed in the later section in terms of Koop's theory.

The activation energy of the grain and grain boundary was obtained by linearly fitting the conductivity data with temperature
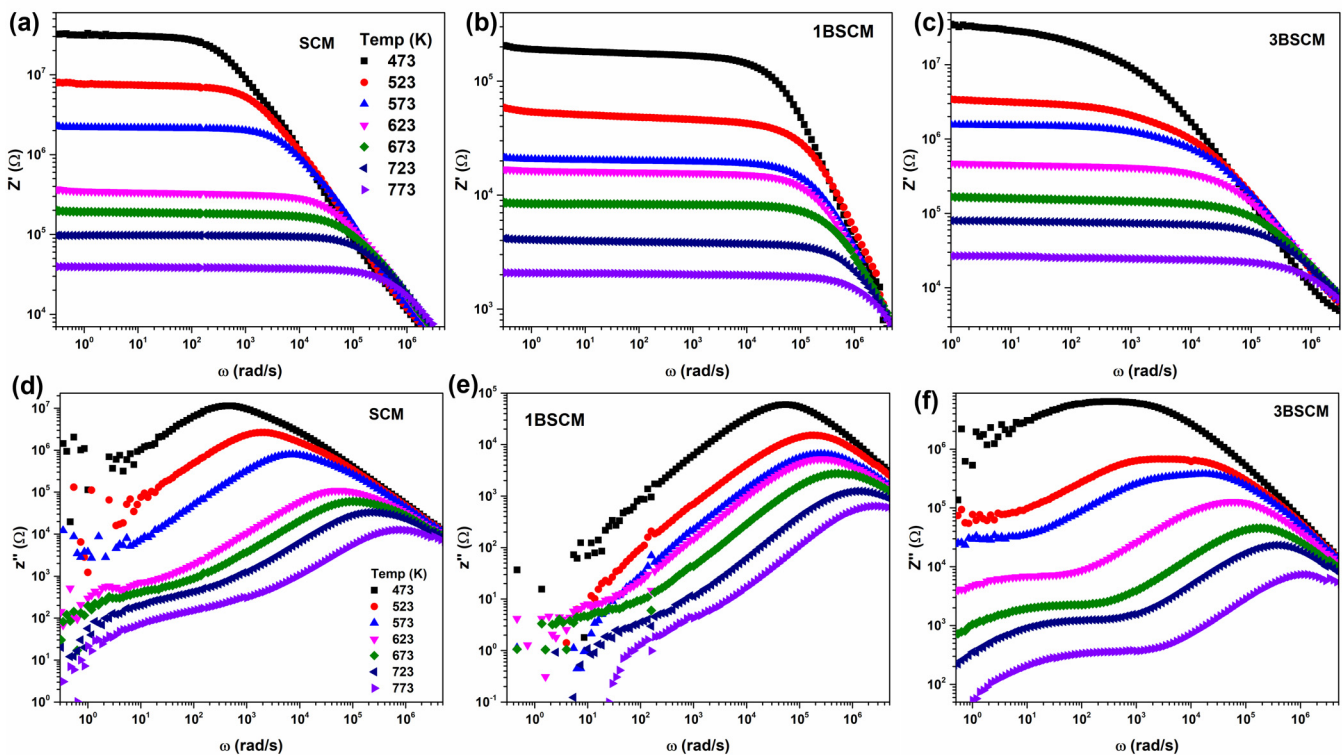
FIG. 4. Spectroscopic plot for variation in [(a)–(c)] the real part (Z′) and [(d)–(f)] imaginary part of impedance (Z″) with frequency in the temperature range of 473–773 K, respectively.

using the Arrhenius equation, which can be given as

$$\sigma = \sigma_0 \exp\left(\frac{-E_a}{K_B T}\right). \quad (7)$$

Here, σ and σ_0 are the conductivity and pre-exponential components, E_a is the activation energy, K_B is the Boltzmann constant (8.617×10^{-5} eV K^{-1}), and T is the absolute temperature. Figures 3(a)–3(c) show the grain (E_g) and grain boundary (E_{gb}) resistance of various samples using the Arrhenius plot. The grain boundary activation energy was found to be higher than the grain activation energy for all compositions. SCM and 3BSCM showed maximum activation energy for the grain of about 0.307 and 0.298 eV and grain boundary of about 0.335 and 0.310 eV, respectively. 1BSCM showed the minimum activation energy for the grain and grain boundary ∼0.178 and 0.195 eV, respectively.

To closely understand the relaxation process in materials, complex impedance data were further studied carefully with frequency and temperature dependence. Figures 4(a)–4(c) show the frequency-dependent Z′ in the temperature range of 473–773 K. The Z′ value was found to be decreasing after the addition of Ba. A constant plateau trend was observed for the Z′ vs frequency plot, which shifted toward a higher frequency with increasing temperature for all cases. The plateau was found to widen with increasing temperature, which is most prominent in x = 0 and 0.3 compositions. Plateau regions signify a frequency-independent pure resistive part of the samples. The decrease in Z′ with the frequency, which eventually merges to a common line at higher frequencies, suggests diminishing space-charge polarization at higher frequencies.[26,42] Moreover, Z′ on the low-frequency region decreases with an increase in temperature, showing a semiconductor-like behavior in oxide ceramics due to the loss of oxygen or oxygen vacancy
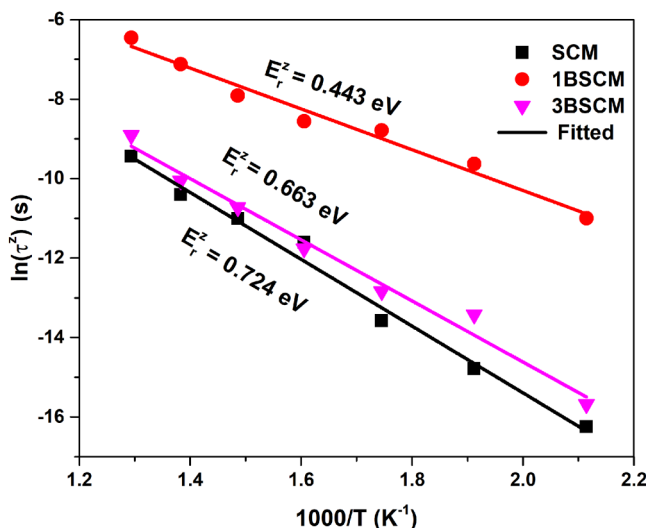

FIG. 5. Arrhenius plot for the relaxation time, τ^z vs 1000/T for the temperature range of 473–773 K.

formation in the lattice.[43] Figures 4(d)–4(f) present the frequency-dependent Z″ plot for all the samples at various temperatures. The peaks in Z″ vs frequency spectra represent a relaxation process. At lower temperatures, the spectrum showed a single peak in the low-frequency region, which shifted toward a higher frequency with the rise in temperature. With the temperature rise, two peaks corresponding to two relaxation processes in high- and low-frequency regions were observed, which was most prominent in the 3BSCM composition. Polaron formation in these double perovskite oxides is expected since transition metals present in the system exhibit multiple oxidation states such as Cr^{3+}, Cr^{6+}, Mo^{5+}, and Mo^{6+}.[44] Therefore, the peak on the high-frequency side may indicate the characterized response from localized hopping of polarons in the grain interior between lattice sites having a characteristic timescale. As the temperature rises, the peak moves away from the low-frequency region, indicating a temperature-dependent phenomenon. The response in the low-frequency range can be triggered by the grain boundaries and electrode polarization.[45] At low temperatures, the grain boundary characteristic peaks are either out of the experimental window or small enough not to be observed distinctly. In the Z″ vs frequency plot, we obtained the characteristic peak frequency or relaxation frequency f_r^z for charge carriers hopping. Furthermore, the relaxation time was calculated using $f_r^z = \frac{1}{2\pi f_r^z}$ which was found to be decreasing with increasing temperature.[43] As the relaxation phenomena of charge carriers hopping are thermally activated, it satisfies the Arrhenius equation, which is given as

$$\tau^z = \tau_0^z \exp^{\frac{E_r^z}{K_B T}}. \quad (8)$$

Here, τ_0^z is a pre-exponential constant, T is absolute temperature, K_B is the Boltzmann constant, and E_r^z is the activation energy for the relaxation mechanism. The obtained slope from fitting the plot between τ^z as a function of the inverse of temperature (1000/T) provides the E_r^z value, as shown in Fig. 5.

C. Electric modulus formalism

The formalization of electric modulus spectroscopy was initially suggested by Macedo et al., which is defined as the inverse of complex dielectric permittivity,[46,47]

$$M^*(\omega) = \frac{1}{\varepsilon^*(\omega)} = \frac{\varepsilon'(\omega)}{\varepsilon'^2(\omega) + \varepsilon'^2(\omega)} + i\frac{\varepsilon''(\omega)}{\varepsilon'^2(\omega) + \varepsilon'^2(\omega)}$$
$$= M'(\omega) + iM''(\omega). \quad (9)$$

This approach is convenient for analyzing different relaxation mechanisms in a polycrystalline material. When using M^* (M'' vs frequency), the peak values are proportional to the reciprocal of capacitance; therefore, low capacitance processes are accentuated. Consequently, the grain effects in the polycrystalline materials are magnified in the modulus plot, as we have shown in Sec. III B that grain boundaries are more capacitive than grains. On the other hand, in impedance formalism (Z″ vs frequency), greater resistive processes are amplified, which means that the grain boundary effects are accentuated.[36] Therefore, the impedance spectra of the
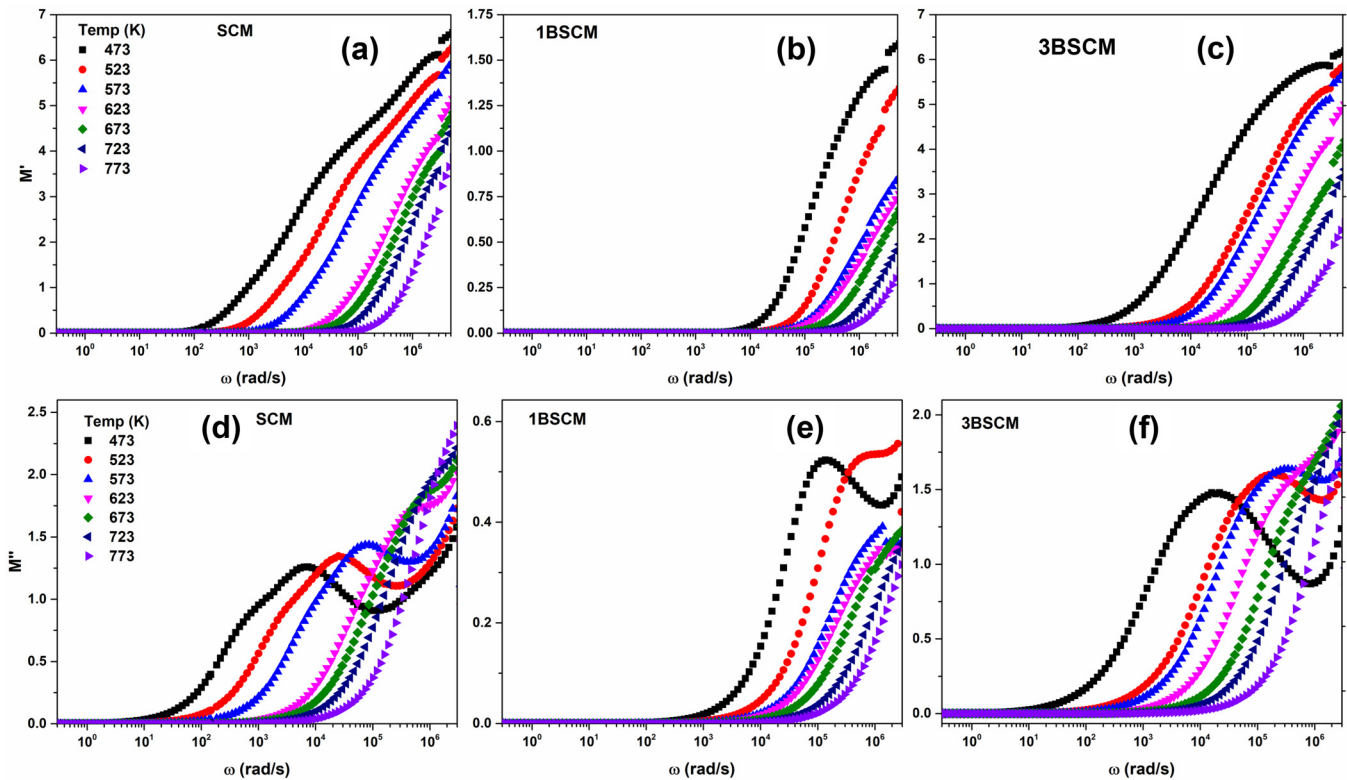
FIG. 6. The variation of [(a)–(c)] the real and [(d)–(f)] imaginary parts of the electric modulus with frequency for the temperature range of 473–773 K.

polycrystalline materials reveal the non-localized long-range conduction activity, whereas the modulus spectra reveal the localized relaxation process.[28] Consequently, the combination of impedance and modulus formalisms is vastly used to distinguish the grain and grain boundary effects and to analyze the various microscopic processes occurring inside a polycrystalline material.[37,45,48] In terms of the resistance and capacitance of the grain and grain boundaries, the real and imaginary modulus can be written as

$$M' = \frac{C_0}{C_g}\left[\frac{(\omega R_g C_g)^2}{1+(\omega R_g C_g)^2}\right] + \frac{C_0}{C_{gb}}\left[\frac{(\omega R_{gb} C_{gb})^2}{1+(\omega R_g C_g)^2}\right] = i\omega C_0 Z'', \quad (10)$$

$$M'' = \frac{C_0}{C_g}\left[\frac{\omega R_g C_g}{1+(\omega R_g C_g)^2}\right] + \frac{C_0}{C_{gb}}\left[\frac{\omega R_{gb} C_{gb}}{1+(\omega R_g C_g)^2}\right] = i\omega C_0 Z'. \quad (11)$$

Figure (6) represents frequency-dependent complex modulus spectra for temperatures range of 473–773 K. The M^* formalism is an excellent tool for polycrystalline ceramic materials to probe the electrical charge transport phenomena such as charge carriers or ions' hopping mechanisms.[49] Figures 6(a)–6(c) show the variation of M' with frequency and temperature, which shows that in

low-frequency regions, the M' value becomes very small and constant. The M' value increases with an increase in frequency, and it decreases with a temperature rise. While increasing with frequency, a dispersive region can be observed, which becomes nearly asymptotic or saturates at high frequencies with the value of M_∞ ($M_\infty = 1/\varepsilon_\infty$).[49] The dispersion phenomena seen on the high-frequency side of the spectrum suggest the presence of charge carriers with a limited range of mobility due to rapidly changing electric fields, which could take place in the grain or bulk of the material.

In Figs. 6(d)–6(f), strong peaks of M'' were observed in the experimental temperature range, which shifted toward higher frequencies with temperature rise. We assigned these peaks to grain relaxation peaks with smaller capacitance. Simultaneously, grain boundary relaxation peaks with much greater capacitance were suppressed, which are, in general, anticipated to be much weaker in peak strength than grain. The nature of M'' spectra was found to be asymmetric about the peak for all temperature ranges, and the response can be categorized into two parts: high- and low-frequency response. The low-frequency response region, which comes before the peak maxima, indicates the presence of long-range mobility of charge carriers. In comparison, the high-frequency response region, which comes after the peak maxima, demonstrates that the charge carriers are rather confined in a potential well, and the mobility is restricted to a short range. The
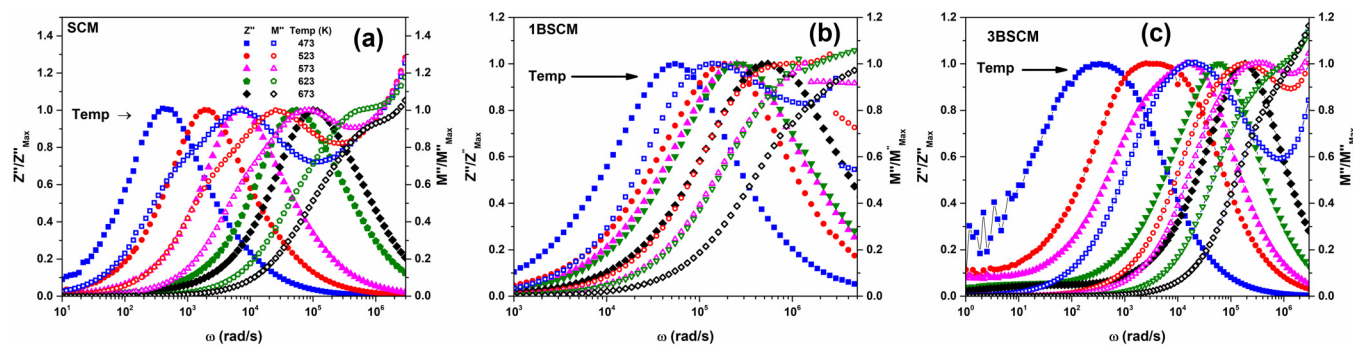
FIG. 7. (a)–(c) The normalized Z'' and M'' vs frequency plot for BSCM double perovskite.

peak area represents the transition from long-range to short-range charge carrier transport.[50]

So far, it has been established that there is a presence of both long- and short-range motion of charge carriers with departure from the Debye-type mechanism. Furthermore, the normalized Z'' and M'' plots are employed to confirm these arguments, as shown in Figs. 7(a)–7(c). The peaks of Z''/Z''_{Max} and M''/M''_{Max} do not coincide, suggesting that the behavior is the non-Debye type and that both long- and short-range transport of charge carriers are contributing to the conduction process.[49] In addition, both peaks

tend to come closer with the temperature rise, suggesting that with increasing temperature, the long-range motion of the charge carrier dominates. This is expected as additional thermal energy to the lattice will promote the mobilization or hopping of charge carriers.

D. Permittivity formalism

The complex dielectric study has often been used to study ionically conducting and disordered materials, e.g., polymers, melts, amorphous semiconductors, and doped crystals.[51–55] The complex dielectric
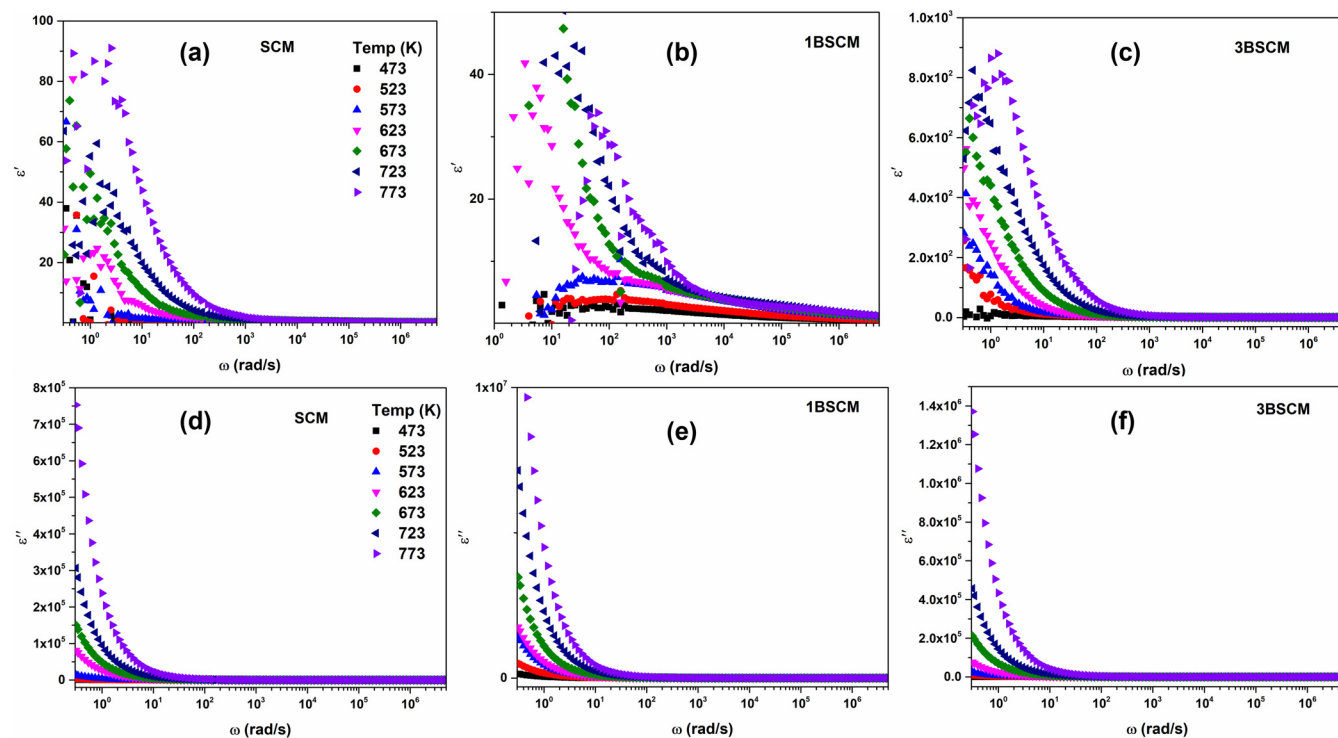
FIG. 8. The frequency-dependent [(a)–(c)] real and [(d)–(f)] imaginary parts of permittivity spectra for the temperature range of 473–773 K.

can be written as Eq. (4), and the loss tangent is given as

$$\tan\delta = \frac{\varepsilon''}{\varepsilon'}. \qquad (12)$$

The real (ε') and imaginary (ε'') parts of complex permittivity are related to impedance values as

$$\varepsilon' = \frac{1}{\omega C_0}\left(\frac{Z''}{Z'^2 + Z''^2}\right) \text{ and } \varepsilon'' = \frac{1}{\omega C_0}\left(\frac{Z'}{Z'^2 + Z''^2}\right). \qquad (13)$$

Figures 8(a)–8(c) and 8(d)–8(f) show the frequency-dependent real and imaginary dielectric spectra at different temperatures. It was observed that at a temperature below 623 K, ε'' and ε' become very small and weakly dependent on frequency. It can be visualized as if the dielectric loss ε'' becomes nearly constant over the entire frequency range on given temperatures. This behavior is often found in ionic melts, crystals, and glasses, where it is referred to as the "near constant loss" (NCL).[28,56,57] In addition, the NCL is regarded as the "universal response" of material next to the "universal dielectric response" (URD).[33] The genesis of NCL is generally regarded as a particle moving in asymmetric double-well potentials.[58] The motion involved in such relaxations is highly localized, as opposed to the dominating hopping process.

It is found that both ε'' and ε' increase monotonically with the rise in temperature and decrease with the increase in frequency. Similar

behavior has been widely reported.[28,37] The phenomenon of the dependence of dielectric permittivity on frequency can be explained by Koop's theory for inhomogeneous systems.[59] This model suggests that the inhomogeneous system consists of two Maxwell–Wagner-type layers in which the conducting regions are separated by non-conducting layers that represent grains and grain boundaries, respectively. The ions and electrons approach the grain boundary by hopping through the grain, and if the resistance of the grain boundary is high enough, they start accumulating on the grain boundary. This gives rise to polarization in the region, and the grain boundary becomes even more resistive and capacitive.[37] Consequently, both ε'' and ε' increases manifold with the rise in temperature at low frequencies. However, as the frequency increases, ε'' and ε' decreases, which can be explained as that the charge carriers move more rapidly about their equilibrium position as opposed to traveling greater distances. This reduces their probability of reaching the grain boundary, resulting in a fall in dielectric permittivity and loss.[28]

E. AC conductivity study

The conductivity of samples was obtained from impedance data using Eq. (14),

$$\sigma' = \frac{\varepsilon_0}{C_0}\frac{Z'}{Z'^2 + Z''^2} = \frac{d}{A}\frac{Z'}{Z'^2 + Z''^2}. \qquad (14)$$

The conductivity in ceramics is dependent on the nature of the grain and grain boundary. We also found in this study that the
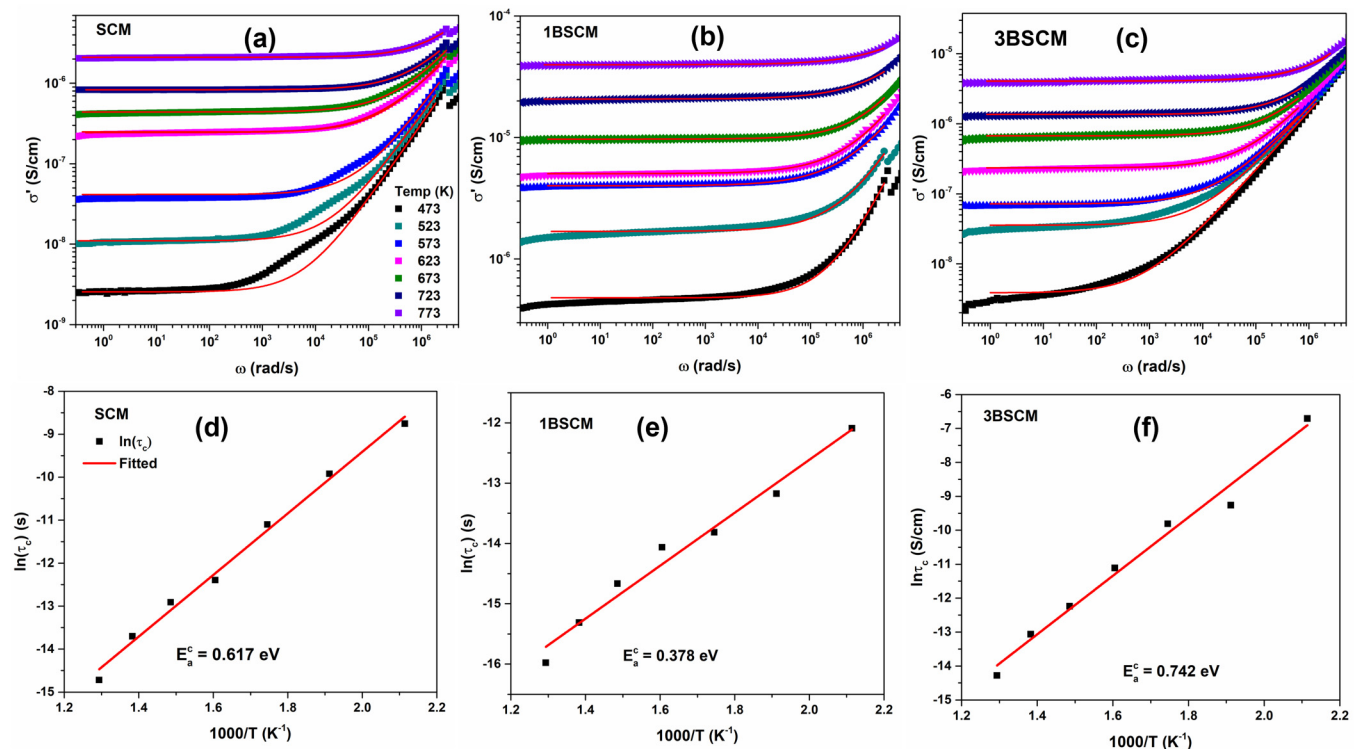
FIG. 9. (a)–(c) The Almond West fitting of ac conductivity data and (d)–(f) the Arrhenius plot between conductivity relaxation and inverse of temperature.

TABLE III. Obtained relaxation frequency and numerical constant p from fitting conductivity data with the AW power law.

Temp. (K)	SCM $\omega_c \times 10^3$ (rad/s)	p	$\sigma_0 \times 10^{-9}$ (S/cm)	1BSCM $\omega_c \times 10^3$ (rad/s)	p	$\sigma_0 \times 10^{-7}$ (S/cm)	3BSCM $\omega_c \times 10^3$ (rad/s)	p	$\sigma_0 \times 10^{-9}$ (S/cm)
473	6.34 ± 0.14	0.95 ± 0.004	2.55 ± 0.0	178 ± 0.0	0.79 ± 0.004	4.67 ± 0.0	0.819 ± 0.0	0.83 ± 0.0007	3.85 ± 0.0
523	20.4 ± 0.691	0.92 ± 0.007	11 ± 0.0	526 ± 0.0	0.77 ± 0.009	16.7 ± 0.1	10.5 ± 0.47	0.82 ± 0.003	39.2 ± 1.0
573	66.3 ± 3.653	0.91 ± 0.009	41.4 ± 1.0	1000 ± 0.0	0.73 ± 0.01	41.3 ± 0.15	18.2 ± 0.40	0.79 ± 0.003	71.7 ± 0.65
623	242 ± 8.658	0.81 ± 0.01	248 ± 2.69	1280 ± 0.0	0.84 ± 0.02	53.6 ± 0.31	67 ± 0.96	0.81 ± 0.004	235 ± 1.0
673	405 ± 9.577	0.79 ± 0.008	439 ± 2.70	2340 ± 0.0	0.72 ± 0	98 ± 0.22	207 ± 4.57	0.78 ± 0.014	674 ± 3.74
723	894 ± 3.574	0.8 ± 0.003	832 ± 0.82	4460 ± 0.0	0.63 ± 0.01	200 ± 0.57	470 ± 7.06	0.77 ± 0.015	1350 ± 4.87
773	2470 ± 30.568	0.8 ± 0.01	2100 ± 3.93	8690 ± 0.0	0.72 ± 0.009	400 ± 0.65	1590 ± 35.84	0.75 ± 0.02	4090 ± 19.1

grain boundaries are more resistive than grains and they work as an insulating barrier around grains. The study of ac conductivity is a well-established method for investigating the charge transport mechanism. It generally shows a dispersive conductivity behavior, i.e., frequency-dependent conductivity. The universal power law for dielectric materials, also known as the universal dielectric response (UDR),[60,61] is the equation that best represents the frequency dependence of conductivity, as given in Eq. (15),

$$\sigma(\omega) = \sigma(0) + A\omega^n. \quad (15)$$

Here, $\sigma(0) = \lim_{\omega \to 0} \sigma(\omega)$ is called DC conductivity, A is a temperature-dependent constant, and if n lies between $0 < n < 1$, it is regarded as a UDR region, as proposed by Jonscher.[61] The second term, $A\omega^n$, represents the dispersion region. As a consequence of Eq. (16), the dielectric loss can be written as

$$\varepsilon'' = [\sigma(\omega) - \sigma(0)]/\varepsilon_0\omega. \quad (16)$$

Clearly, the power law becomes invalid as $\omega \to 0$.[56] Almond and West (AW) derived a more convenient formalism that not just describes UDR behavior but also incorporates hopping frequency ω_c. The relation[62,63] is given by Eq. (20),

$$\sigma(\omega) = \sigma(0)[1 + (\omega\tau)^p] = \sigma(0)\left[1 + \left(\frac{\omega}{\omega_c}\right)^p\right], \quad (17)$$

where τ_c is called the conductivity relaxation time, with the assumption that $\omega_c = \tau_c^{-1}$, and p is a numerical constant of order one.

TABLE IV. Activation energy obtained from different formalisms.

Composition/activation energy (eV)	SCM	1BSCM	3BSCM
AW formalism	0.617 ± 0.02	0.378 ± 0.02	0.742 ± 0.04
Nyquist fitting	0.617 ± 0.02	0.373 ± 0.02	0.633 ± 0.02
Relaxation phenomena	0.724 ± 0.03	0.443 ± 0.03	0.663 ± 0.03

Figures 9(a)–9(c) show the frequency-dependent conductivity for the temperature range of 473–773 K. The obtained curve can be divided into three regions. First is the plateau in the low-frequency region representing DC conductivity which is thermally activated and increases with temperature. The origin of $\sigma(0)$ is mainly by the long-distance mobility of ionic particles. The second region represents dispersion with onset at the crossover frequency ω_c. Eventually, the curve becomes linear, indicating the third region. The ac conductivity data have fitted with the AW power law in which the value of $\sigma(0)$, exponent p, and hopping or crossover frequency ω_c were extracted. $\sigma(0)$ and p were found to increase with temperature rise. The obtained values of $\sigma(0)$, p, and ω_c are listed in Table III. As DC conductivity is thermally activated, at higher temperatures, it becomes dominant, suggesting the delocalization of charge carriers in the grain and grain boundary region.[37] ω_c was observed to increase monotonically with temperature, i.e., ω_c
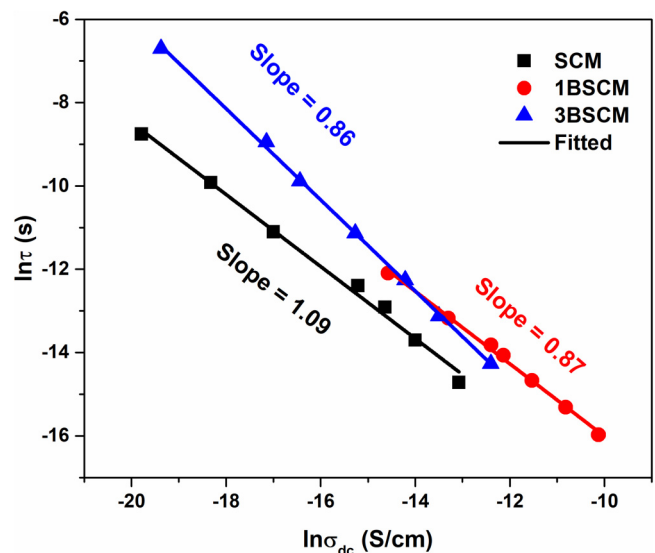

FIG. 10. The plot between $\ln(\tau)$ and $\ln \sigma_{dc}$ that shows the BNN relation for various samples.
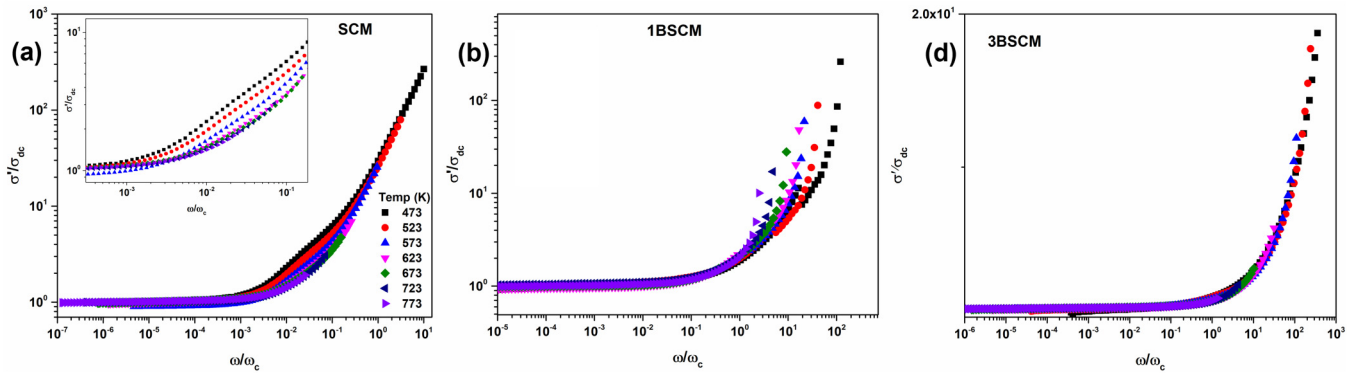
FIG. 11. The conductivity time-temperature superposition (TTSP) scaling behavior of (a) SCM, (b) 1BSCM, and (c) 3BSCM.

$(\tau_c = 1/\omega_c)$ is temperature-dependent. The temperature-dependent relaxation time can be given by the following Arrhenius Eq. (18):

$$\tau_c = \tau_0 \exp\left(\frac{E_a^c}{KT}\right). \qquad (18)$$

Figures 9(d)–9(f) show the plot between $\ln(\tau_c)$ and 1000/T. Their slope gives the activation energy, E_a^c.

Conductivity is found to increase with Ba-doping in SCM composition and a decrease in activation energy is simultaneously observed. The activation energy obtained for 1BSCM was found to be lower than SCM and 3BSCM for all formalisms. However, for the SCM and 3BSCM composition, the activation energy was found to be nearly the same. The error in values can originate from errors in fitting, overestimating, or underestimating the activation energy. Nevertheless, the activation energy obtained from AW formalism [Eq. (18)], relaxation *of the hopping* mechanism [Eq. (8)], and Nyquist fitting [Eq. (7)] are close to each other, which suggests

that the same charge carriers are responsible for the relaxation and conduction mechanism in the material.[41] Table IV shows the obtained values of activation energy from these formalisms.

F. BNN relation

Barton,[30] Nakajima,[31] and Namikawa[32] (BNN) gave an empirical relation between DC conductivity $\sigma(0)$ and hopping frequency ω_c, which is given by Eq. (19),

$$\sigma(0) = p\varepsilon_0\Delta\varepsilon\omega_c \Rightarrow \sigma(0) \propto \omega_c, \qquad (19)$$

where $\Delta\varepsilon = \varepsilon_0 - \varepsilon_\infty$ is the relaxation strength. Equation (19) is regarded as the BNN relation.[37] It suggests that the hopping frequency is proportional to the DC conductivity and has the same activation energy.[64] When working with disordered substances with high carrier concentrations, the BNN relation might be useful. This relation follows in most disordered solids where migrating charge carriers dominate than dipolar loss, which is also of interest
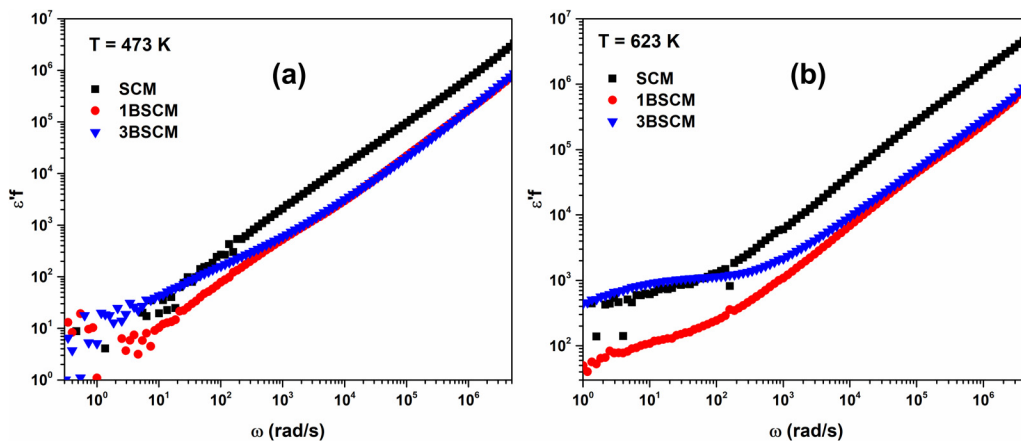

FIG. 12. Kramers–Kronig analysis of BSCM double perovskites at (a) 473 and (b) 623 K.

here.[65] Figure 10 shows the BNN plot between $\ln(\tau)$ and $\ln \sigma_{dc}$, the straight line indicates that this relation is followed, and migration type charge transport is dominated in the materials.

G. Scaling of AC conductivity and time-temperature superposition theorem (TTSP)

Scaling of acquired distinct physical data sets by a certain parameter is an effective method for separating diverse common processes by collapsing them into a single master curve, independent of their composition or any short- or long-range interactions.[57,66] As demonstrated in AC conductivity analysis, the crossover frequency increases or shifts to a higher frequency as the temperature rises, completely separating the DC and dispersion regions. It shows that it is possible to scale the conductivity with DC conductivity and the crossover frequency. There have been several approaches reported on the scaling of conductivity. For example, Roling et al. have proposed the scaling of conductivity by using $\sigma_{dc}T$ as a scaling factor.[66] He also incorporated the mole fraction, x, into the scaling factor $\sigma_{dc}T/x$ when dealing with various compositions. Later, Sidebottom et al. showed the fallacy of the earlier approach and proposed a modified scaling factor $\sigma_0/\varepsilon_0\Delta\varepsilon$.[57] Ghosh and Pan et al. have presented a rigorous discussion on conductivity scaling in ionic solids.[34] They have demonstrated that scaling with a crossover frequency of the frequency axis is a better approach as the crossover frequency is not restricted to a composition range or types of material. Therefore, the scaling of conductivity across the non-NCL region can be given as

$$\frac{\sigma'}{\sigma_{dc}} = F\left(\frac{\omega}{\omega_c}\right), \tag{20}$$

where F is a temperature-independent scaling function. σ' is the real part of complex conductivity σ^* and σ_{dc} is the DC conductivity. ω and ω_c are the angular frequency and crossover frequency, respectively. It was observed that the scaling of conductivity in the low-frequency region lies nearly on a single curve, as shown in Fig. 11. However, a dispersion can also be observed toward the higher frequency that deviates from collapsing to a single curve. As the form of the curve does not change but merely shifts with temperature, it justifies the time-temperature superposition theorem.[34,57,66]

H. Kramers Kronig transformation (KKT)

As discussed earlier, ε' and ε'' decrease rapidly with a lowering in temperature and becomes nearly constant at lower temperatures, i.e., from the UDR to NCL, behavior begins to dominate. From the Kramers Krönig formalism, ε' is related to the real part of conductivity σ' by the relation $\varepsilon'f = Bf^m$.

Therefore, it can be rewritten as[37,67]

$$\varepsilon' = Bf^{m-1}, \tag{21}$$

where f represents frequency and B is a constant. The exponent m is obtained from the slope between the log–log plot of $\varepsilon'f$ and f. Figures 12(a) and 2(b) show the KKT plot at low temperature (473 K) and high temperature (623 K), respectively. The graphs

obtained are nearly linear at both temperatures. Interestingly, it was found that the value of m obeys a decreasing trend with temperature rise. The valuable of m lies between 0.84 and 0.90 at a lower temperature which decreases to 0.70–0.82 at a higher temperature. It confirms our earlier observations that the behavior at low temperatures is of the NCL type, which transforms to URD with the temperature rise.

IV. CONCLUSION

In summary, we investigated the charge transport mechanism in Ba-doped Sr_2CrMoO_6 double perovskites using impedance, dielectric, and modulus spectroscopy. The impedance analysis revealed an increase in the conductivity of SCM after Ba-doping. Furthermore, the Nyquist fitting showed that the grain and grain boundary resistivity decreased with increasing temperature. The maximum grain and grain boundary conductivity obtained was 0.1 and 0.07 mS cm^{-1} at 773 K, respectively, for $Ba_xSr_{2-x}CrMoO_6$ (x = 0.1) composition. The conductivity data were examined with the AW power law which suggests the presence of the hopping mechanism of charge carriers and relaxation follows the temperature-dependent Arrhenius behavior. Furthermore, both long- and short-range charge carrier transport contributed to the conduction process. The normalized Z″ and M″ spectra revealed a non-Debye-type relaxation. The scaling behavior of conductivity was examined, which lies on a single master curve and obeys TTSP. The Kramers–Kronig analysis further validated the impedance data.

AUTHOR DECLARATIONS

Conflict of Interest

The authors have no conflicts to disclose.

Author Contributions

Vivek Kumar: Data curation (equal); Formal analysis (equal); Investigation (lead); Methodology (lead); Writing – original draft (lead); Writing – review & editing (equal). **Sudha Saini:** Investigation (equal); Methodology (equal). **Tanmoy Maiti:** Conceptualization (lead); Formal analysis (lead); Funding acquisition (lead); Investigation (equal); Project administration (lead); Resources (lead); Supervision (lead); Writing – review & editing (lead).

DATA AVAILABILITY

The data that support the findings of this study are available within the article.

REFERENCES

[1]S. Y. Kim and J. Li, "Porous mixed ionic electronic conductor interlayers for solid-state batteries," Energy Mater. Adv. **2021**, 1 (2021).

[2]M. L. Picchio, A. Gallastegui, N. Casado, N. Lopez-Larrea, B. Marchiori, I. del Agua, M. Criado-Gonzalez, D. Mantione, R. J. Minari, and D. Mecerreyes, "Mixed ionic and electronic conducting eutectogels for 3D-printable wearable sensors and bioelectrodes," Adv. Mater. Technol. **7**(10), 2101680 (2022).

[3]E.-K. Lee, S.-A. Park, H.-W. Jung, and Y.-T. Kim, "Performance enhancement of molten carbonate-based direct carbon fuel cell (MC-DCFC) via adding mixed ionic-electronic conductors into Ni anode catalyst layer," J. Power Sources **386**, 28–33 (2018).

[4]Y. Cao, Z. Zhu, Y. Zhao, W. Zhao, Z. Wei, and T. Liu, "Development of tungsten stabilized $SrFe_{0.8}W_{0.2}O_{3-\delta}$ material as novel symmetrical electrode for solid oxide fuel cells," J. Power Sources **455**, 227951 (2020).

[5]C. Acar and I. Dincer, "Comparative assessment of hydrogen production methods from renewable and non-renewable sources," Int. J. Hydrogen Energy **39**(1), 1–12 (2014).

[6]H. C. Maru, S. C. Singhal, C. Stone, and D. Wheeler, "1–10 KW stationary combined heat and power systems status and technical potential: Independent review," NREL/BK-6A10-48265, 2010, p. 993647.

[7]S. Futamura, Y. Tachikawa, J. Matsuda, S. M. Lyth, Y. Shiratori, S. Taniguchi, and K. Sasaki, "Alternative Ni-impregnated mixed ionic-electronic conducting anode for SOFC operation at high fuel utilization," J. Electrochem. Soc. **164**(10), F3055 (2017).

[8]L. Jiang, T. Wei, and Y. Huang, "Review—Double-perovskite electrode design strategies and research progress for SOFCs," J. Electrochem. Soc. **169**(6), 064508 (2022).

[9]S. Afroze, A. Karim, Q. Cheok, S. Eriksson, and A. K. Azad, "Latest development of double perovskite electrode materials for solid oxide fuel cells: A review," Front. Energy **13**(4), 770–797 (2019).

[10]Q. F. Li, X. F. Zhu, and L. F. Chen, "First-principles investigations of disorder effects on electronic structure and magnetic properties in Sr_2CrMoO_6," J. Phys.: Condens. Matter **20**(25), 255230 (2008).

[11]S. Saini, M. Saxena, T. Bhattacharya, A. Saha, and T. Maiti, "Enhanced thermoelectric power factor led by isovalent substitution in Sr_2CrMoO_6 double perovskite," J. Phys. Appl. Phys. **55**(41), 415501 (2022).

[12]Z.-C. Wang, L. Chen, S.-S. Li, J.-S. Ying, F. Tang, G.-Y. Gao, Y. Fang, W. Zhao, D. Cortie, X. Wang, and R.-K. Zheng, "Giant linear magnetoresistance in half-metallic Sr_2CrMoO_6 thin films," npj Quantum Mater. **6**(1), 1–8 (2021).

[13]O. El rhazouani and A. Slassi, "Low field magnetocaloric effect in the double perovskite Sr_2CrMoO_6: Monte Carlo simulation," Comput. Condens. Matter **11**, 55–59 (2017).

[14]D. M. Hoat, "Improving the calculations of electronic and magnetic properties of Sr_2CrMoO_6 double-perovskite with LDA + U and mBJ potential," J. Electron. Mater. **48**(10), 6406–6413 (2019).

[15]X. Yang, J. Liu, F. Chen, Y. Du, A. Deibel, and T. He, "Molybdenum-based double perovskites $A_2CrMoO_{6-\delta}$ (A = Ca, Sr, Ba) as anode materials for solid oxide fuel cells," Electrochim. Acta **290**, 440–450 (2018).

[16]C. M. Chanquía, J. E. Vega-Castillo, A. L. Soldati, H. Troiani, and A. Caneiro, "Synthesis and characterization of pure-phase $La_{0.75}Sr_{0.25}Cr_{0.5}Mn_{0.5}O_{3-\delta}$ nanocrystallites for solid oxide fuel cell applications," J. Nanoparticle Res. **14**(9), 1104 (2012).

[17]S. Tao and J. T. S. Irvine, "A redox-stable efficient anode for solid-oxide fuel cells," Nat. Mater. **2**(5), 320–323 (2003).

[18]T. Wei, Y. Ji, X. Meng, and Y. Zhang, "$Sr_2NiMoO_{6-\delta}$ as anode material for $LaGaO_3$-based solid oxide fuel cell," Electrochem. Commun. **10**(9), 1369–1372 (2008).

[19]S. Presto, P. Kumar, S. Varma, M. Viviani, and P. Singh, "Electrical conductivity of NiMo-based double perovskites under SOFC anodic conditions," Int. J. Hydrogen Energy **43**(9), 4528–4533 (2018).

[20]Y.-F. Sun, Y.-Q. Zhang, B. Hua, Y. Behnamian, J. Li, S.-H. Cui, J.-H. Li, and J.-L. Luo, "Molybdenum doped $Pr_{0.5}Ba_{0.5}MnO_{3-\delta}$ (Mo-PBMO) double perovskite as a potential solid oxide fuel cell anode material," J. Power Sources **301**, 237–241 (2016).

[21]Z. Ma, X. Yuan, L. Li, and Z.-F. Ma, "The double perovskite oxide $Sr_2CrMoO_{6-\delta}$ as an efficient electrocatalyst for rechargeable lithium air batteries," Chem. Commun. **50**(94), 14855–14858 (2014).

[22]G. Dimitri Ngantso, M. Boujnah, A. Benyoussef, and A. El Kenz, "The itinerant magnetism in a 3d-4d double perovskite Sr_2CrMoO_6," J. Magn. Magn. Mater. **444**, 243–248 (2017).

[23]C. M. Bonilla, D. A. Landínez Téllez, J. Arbey Rodríguez, E. Vera López, and J. Roa-Rojas, "Half-metallic behavior and electronic structure of Sr_2CrMoO_6 magnetic system," Physica B **398**(2), 208–211 (2007).

[24]S. Bhattacharya, "AC conductivity behaviour and charge carrier concentrations of some vanadate glassy system," Phys. Lett. A **384**(16), 126324 (2020).

[25]T. Dam, S. N. Tripathy, M. Paluch, S. S. Jena, and D. K. Pradhan, "Investigations of relaxation dynamics and observation of nearly constant loss phenomena in $PEO_{20}-LiCF_3SO_3-ZrO_2$ based polymer nano-composite electrolyte," Electrochim. Acta **202**, 147–156 (2016).

[26]K. C. Varada Rajulu, B. Tilak, and K. Sambasiva Rao, "Impedance spectroscopy study of BNKLT polycrystalline ceramic," Appl. Phys. A **106**(3), 533–543 (2012).

[27]D. P. Almond, C. C. Hunter, and A. R. West, "The extraction of ionic conductivities and hopping rates from A.C.: Conductivity data," J. Mater. Sci. **19**(10), 3236–3248 (1984).

[28]R. Tang, C. Jiang, W. Qian, J. Jian, X. Zhang, H. Wang, and H. Yang, "Dielectric relaxation, resonance and scaling behaviors in $Sr_3Co_2Fe_{24}O_{41}$ hexaferrite," Sci. Rep. **5**(1), 13645 (2015).

[29]R. Kaur, A. Kaur, and A. Singh, "Electrical relaxation and conduction behaviour in $SmFeO_3$ modified $PbZrTiO_3$ ceramics," J. Mater. Sci. Mater. Electron. **33**(31), 24295–24307 (2022).

[30]J. L. Barton, "Dielectric relaxation of some ternary alkali-alkaline earth-silicate glasses," Verres Refract. **20**(5), 328–335 (1966).

[31]T. Nakajima, "Correlation between electrical conduction and dielectric polarization in inorganic glasses," in *Conference on Electrical Insulation & Dielectric Phenomena* (IEEE, Piscataway, NJ, 1971), pp. 168–176.

[32]H. Namikawa, "Characterization of the diffusion process in oxide glasses based on the correlation between electric conduction and dielectric relaxation," J. Non-Cryst. Solids **18**(2), 173–195 (1975).

[33]W. K. Lee, J. F. Liu, and A. S. Nowick, "Limiting behavior of ac conductivity in ionically conducting crystals and glasses: A new universality," Phys. Rev. Lett. **67**(12), 1559–1561 (1991).

[34]A. Ghosh and A. Pan, "Scaling of the conductivity spectra in ionic glasses: Dependence on the structure," Phys. Rev. Lett. **84**(10), 2188–2190 (2000).

[35]J. Rodriguez-Carvajal, *Program FULLPROF* (Lab. Léon Brillouin CEA-CNRS Version 3, 1990).

[36]I. M. Hodge, M. D. Ingram, and A. R. West, "Impedance and modulus spectroscopy of polycrystalline solid electrolytes," J. Electroanal. Chem. Interfacial Electrochem. **74**(2), 125–143 (1976).

[37]S. Saini, K. Balani, and T. Maiti, "The analysis of charge transport mechanism in mixed ionic electronic conductor composite of Sr_2TiCoO_6 double perovskite with yttria stabilized zirconia," J. Phys.: Condens. Matter **33**(31), 315703 (2021).

[38]C. Schneider, W. Rasband, and K. Eliceiri, "NIH image to ImageJ: 25 years of image analysis," Nat. Methods **9**, 671–675 (2012).

[39]M. M. Musiani, "Characterization of electroactive polymer layers by electrochemical impedance spectroscopy (EIS)," Electrochim. Acta **35**(10), 1665–1670 (1990).

[40]A. S. Bondarenko and G. A. Ragoisha, "EIS spectrum analyser," EIS Spectr. Anal. Beta Release, http://www.abc.chemistry.bsu.by/vi/analyser/ (2008).

[41]A. Kumar, B. P. Singh, R. N. P. Choudhary, and A. K. Thakur, "Characterization of electrical properties of Pb-modified $BaSnO_3$ using impedance spectroscopy," Mater. Chem. Phys. **99**(1), 150–159 (2006).

[42]J. Suchanicz, "The low-frequency dielectric relaxation $Na_{0.5}Bi_{0.5}TiO_3$ ceramics," Mater. Sci. Eng. B **55**(1), 114–118 (1998).

[43]R. Bellouz, S. Kallel, K. Khirouni, O. Pena, and M. Oumezzine, "Structural, electrical conductance and complex impedance analysis of $(Nd_{1-x}Ce_x)_{0.7}Sr_{0.3}-MnO_3$ ($0 \leq x \leq 0.20$) perovskite," Ceram. Int. **41**(2, Part A), 1929–1936 (2015).

[44]T. Maiti, M. Saxena, and P. Roy, "Double perovskite $(Sr_2B'B''O_6)$ oxides for high-temperature thermoelectric power generation—A review," J. Mater. Res. **34**(1), 107–125 (2019).

[45]T. Lakshmana Rao, M. K. Pradhan, S. Singh, and S. Dash, "Influence of Zn(II) on the structure, magnetic and dielectric dynamics of nano-LaFeO$_3$," J. Mater. Sci. Mater. Electron. **31**(6), 4542–4553 (2020).

[46]P. B. Macedo, and M. CT, "The role of ionic diffusion in polarisation in vitreous ionic conductors," Phys. Chem. Glasses **13**, 171–179 (1972).

[47]J. R. Macdonald, "Impedance spectroscopy," Ann. Biomed. Eng. **20**(3), 289–305 (1992).

[48]J. Liu, C.-G. Duan, W.-G. Yin, W. N. Mei, R. W. Smith, and J. R. Hardy, "Large dielectric constant and Maxwell-Wagner relaxation in Bi$_{2/3}$Cu$_3$Ti$_4$O$_{12}$," Phys. Rev. B **70**(14), 144106 (2004).

[49]S. Sharma, K. Shamim, A. Ranjan, R. Rai, P. Kumari, and S. Sinha, "Impedance and modulus spectroscopy characterization of lead free barium titanate ferroelectric ceramics," Ceram. Int. **41**(6), 7713–7722 (2015).

[50]C. Rayssi, M. Jebli, S. Bouzidi, J. Dhahri, H. Belmabrouk, and A. Bajahzar, "Impedance analysis and modulus behavior of Ca$_{0.85}$Er$_{0.1}$Ti$_{(1-x)}$Co$_{4x/3}$O$_3$ (x = 0.15 and 0.20) ceramic prepared by sol–gel reaction," Appl. Phys. A **128**(5), 435 (2022).

[51]S. Havriliak and S. Negami, "A complex plane representation of dielectric and mechanical relaxation processes in some polymers," Polymer **8**, 161–210 (1967).

[52]R. R. Nigmatullin, A. A. Arbuzov, F. Salehli, A. Giz, and H. Catalgil-Giz, "Experimental confirmation of oscillating properties of the complex conductivity: Dielectric study of polymerization/vitrification reaction," J. Non-Cryst. Solids **353**(44), 4143–4156 (2007).

[53]S. Choudhary and R. J. Sengwa, "Dielectric dispersion and relaxation studies of melt compounded poly(ethylene oxide)/silicon dioxide nanocomposites," Polym. Bull. **72**(10), 2591–2604 (2015).

[54]F. Xiong, Y. Y. Wang, and R. P. H. Chang, "Complex dielectric function of amorphous diamond films deposited by pulsed-excimer-laser ablation of graphite," Phys. Rev. B **48**(11), 8016–8023 (1993).

[55]A. Rouahi, A. Kahouli, F. Challali, M. P. Besland, C. Vallée, B. Yangui, S. Salimy, A. Goullet, and A. Sylvestre, "Impedance and electric modulus study of amorphous TiTaO thin films: Highlight of the interphase effect," J. Phys. Appl. Phys. **46**(6), 065308 (2013).

[56]A. S. Nowick, A. V. Vaysleyb, and I. Kuskovsky, "Universal dielectric response of variously doped CeO$_2$ ionically conducting ceramics," Phys. Rev. B **58**(13), 8398–8406 (1998).

[57]D. L. Sidebottom, "Universal approach for scaling the ac conductivity in ionic glasses," Phys. Rev. Lett. **82**(18), 3653–3656 (1999).

[58]S. Estalji, O. Kanert, J. Steinert, H. Jain, and K. L. Ngai, "Uncommon nuclear-spin relaxation in fluorozirconate glasses at low temperatures," Phys. Rev. B: Condens. Matter **43**(10), 7481–7486 (1991).

[59]C. G. Koops, "On the dispersion of resistivity and dielectric constant of some semiconductors at audiofrequencies," Phys. Rev. **83**(1), 121–124 (1951).

[60]A. K. Johnscher, in *1991 Proceedings of the 3rd International Conference on Properties and Applications of Dielectric Materials* (IEEE, 1991), Vol. 1, pp. 1–11.

[61]A. K. Jonscher, "The 'universal' dielectric response," Nature **267**(5613), 673–679 (1977).

[62]D. P. Almond and A. R. West, "Mobile ion concentrations in solid electrolytes from an analysis of A.C.: Conductivity," Solid State Ion. **9–10**, 277–282 (1983).

[63]D. P. Almond and A. R. West, "Impedance and modulus spectroscopy of 'real' dispersive conductors," Solid State Ion. **11**(1), 57–64 (1983).

[64]J. C. Dyre, "On the mechanism of glass ionic conductivity," J. Non-Cryst. Solids **88**(2), 271–280 (1986).

[65]J. C. Dyre, "Some remarks on ac conduction in disordered solids," J. Non-Cryst. Solids **135**(2–3), 219–226 (1991).

[66]B. Roling, A. Happe, K. Funke, and M. D. Ingram, "Carrier concentrations and relaxation spectroscopy: New information from scaling properties of conductivity spectra in ionically conducting glasses," Phys. Rev. Lett. **78**(11), 2160–2163 (1997).

[67]S. Ke, H. Huang, L. Ren, and Y. Wang, "Nearly constant dielectric loss behavior in poly(3-hydroxybutyrate-co-3-hydroxyvalerate) biodegradable polyester," J. Appl. Phys. **105**(9), 096103 (2009).